

## Article

# Optimization of a Gorlov Helical Turbine for Hydrokinetic Application Using the Response Surface Methodology and Experimental Tests

Juan Camilo Pineda <sup>1</sup>, Ainhoa Rubio-Clemente <sup>1,2</sup> and Edwin Chica <sup>1,\*</sup>

<sup>1</sup> Grupo de Energía Alternativa, Facultad de Ingeniería, Universidad de Antioquia, Calle 70 No. 52-21, Medellín 050010, Colombia; ainhoa.rubioc@udea.edu.co (A.R.-C.)

<sup>2</sup> Escuela Ambiental, Facultad de Ingeniería, Universidad de Antioquia, Calle 70 No. 52-21, Medellín 050010, Colombia

\* Correspondence: edwin.chica@udea.edu.co; Tel.: +57-604-219-5550

**Abstract:** The work presents an analysis of the Gorlov helical turbine (GHT) design using both computational fluid dynamics (CFD) simulations and response surface methodology (RSM). The RSM method was applied to investigate the impact of three geometric factors on the turbine's power coefficient ( $C_p$ ): the number of blades ( $N$ ), helix angle ( $\gamma$ ), and aspect ratio (AR). Central composite design (CCD) was used for the design of experiments (DOE). For the CFD simulations, a three-dimensional computational domain was established in the Ansys Fluent software, version 2021R1 utilizing the  $k-\omega$  SST turbulence model and the sliding mesh method to perform unsteady flow simulations. The objective function was to achieve the maximum  $C_p$ , which was obtained using a high-correlation quadratic mathematical model. Under the optimum conditions, where  $N$ ,  $\gamma$ , and AR were 5,  $78^\circ$ , and 0.6, respectively, a  $C_p$  value of 0.3072 was achieved. The optimal turbine geometry was validated through experimental testing, and the  $C_p$  curve versus tip speed ratio (TSR) was determined and compared with the numerical results, which showed a strong correlation between the two sets of data.

**Keywords:** computational fluid dynamics; response surface methodology; optimization; Gorlov helical turbine; power coefficient



**Citation:** Pineda, J.C.; Rubio-Clemente, A.; Chica, E. Optimization of a Gorlov Helical Turbine for Hydrokinetic Application Using the Response Surface Methodology and Experimental Tests. *Energies* **2024**, *17*, 5747. <https://doi.org/10.3390/en17225747>

Academic Editor: Francesco Castellani

Received: 18 October 2024  
Revised: 7 November 2024  
Accepted: 15 November 2024  
Published: 17 November 2024



**Copyright:** © 2024 by the authors. Licensee MDPI, Basel, Switzerland. This article is an open access article distributed under the terms and conditions of the Creative Commons Attribution (CC BY) license (<https://creativecommons.org/licenses/by/4.0/>).

## 1. Introduction

Electric power is a fundamental requirement for fulfilling the basic needs of people, facilitating production processes, and driving social and economic development. For several decades, 85% of primary energy has been derived from fossil fuels [1–3]. However, the depletion of global oil reserves, the escalation of climate change, and the detrimental environmental effects of conventional energy generation have stimulated the search for clean, adaptable, and dependable systems for energy production [1,2,4]. To this end, it is essential to explore alternative sources of electricity for remote and rural regions. Hydrokinetic turbines and low-head hydraulic turbines are promising solutions that can enable micro- or pico-hydroelectric power generation in these areas [5–8]. By harnessing the energy of flowing water, these renewable technologies offer environmentally friendly and cost-effective ways to generate electricity and improve the quality of life in under-served regions [5,8–10].

Hydrokinetic turbines offer an innovative way to harness the kinetic energy of water currents, whether in natural or artificial channels, and even in ocean currents, for electricity generation. There are two main types of hydrokinetic turbines: horizontal-axis and vertical-axis turbines [5–7,10]. While most research has focused on horizontal-axis turbines, vertical-axis turbines have their own advantages, such as design simplicity, ease of assembly and disassembly, low noise emissions, and the ability to operate in any flow direction.

The most common types of vertical-axis turbines are the Savonius, the H Darrieus, and the Gorlov turbines [6,7,10]. Despite the promising benefits, commercialization of these turbines still faces obstacles such as high energy transformation costs, optimization of individual turbines and their arrangements, balancing energy extraction with environmental impacts, and addressing socio-economic factors linked to the implementation process. Therefore, there is a clear need to explore new configurations, optimize existing geometries, and even design new geometries to increase efficiency and reduce energy costs. By addressing these challenges, vertical-axis hydrokinetic turbines can become a competitive alternative to conventional energy sources, helping to meet growing energy demand while also promoting sustainable development [5–7,11].

The Gorlov helical turbine (GHT) is a promising solution for hydrokinetic power generation. Its design, developed by Alexander Gorlov in the 1990s, includes a helical curvature of the blades that reduces some of the instabilities present in other vertical-axis turbines [7,12]. The unique shape of the turbine ensures that at each angle of rotation it can have a surface with multiple angles of attack, allowing for higher efficiencies. This is achieved by the blades completely covering the outer circumference of the turbine, unlike other turbines where the blades are placed on one side of the rotor. The reliability and efficiency of the GHT has been demonstrated in laboratory tests and field tests in the Cape Cod Canal in Massachusetts, where it achieved an efficiency of up to 35% [12]. The GHT's innovative design presents a viable alternative to conventional turbines for hydrokinetic power generation, and further research and development in this area has the potential to contribute significantly to the transition to clean energy sources [8,10,13].

The Gorlov helical turbine, while showing great promise, still faces several developmental challenges that must be addressed for broader adoption and commercial viability. First, efficiency optimization is key. Though the turbine already offers higher efficiency than some traditional designs, further research is needed to maximize energy capture in varying water flow conditions, particularly in slow or turbulent currents. This includes refining the blade design and materials to reduce drag and improve energy conversion rates. Improving performance across a range of water speeds and conditions is essential to increase its competitiveness with other renewable energy technologies [13,14].

In addition to efficiency, durability and corrosion resistance in harsh marine environments are critical challenges. The turbine's materials must withstand constant exposure to saltwater, biofouling, and mechanical stress over long periods. Developing advanced, lightweight, and corrosion-resistant materials such as composites or special alloys, could extend the turbine's operational life and reduce maintenance needs. Addressing these durability issues is essential for minimizing downtime and maintenance costs, which can be prohibitive in large-scale marine energy installations [13–15].

Another key challenge is scalability and integration into larger energy systems. For the Gorlov turbine to be viable in commercial projects, it must integrate seamlessly with existing grid infrastructure and compete economically with established renewable energy sources like wind and solar. This requires not only improving the turbine's performance but also developing cost-effective manufacturing techniques that can be scaled up for mass production. Reducing the overall cost of energy generated by these turbines will be a major factor in their broader adoption. Finally, long-term field testing and real-world data collection are necessary to validate the turbine's performance and reliability over time. Extensive testing in diverse environmental conditions would provide critical insights into how the turbine behaves in the long term and allow for data-driven design improvements. Support for ongoing pilot projects and international collaboration in research and development can help accelerate these advancements, paving the way for the Gorlov turbine to play a significant role in the global renewable energy landscape [13–15].

The goal of this study was to improve the performance of the Gorlov helical turbine (GHT) by optimizing its design. To achieve this objective, response surface methodology (RSM) and computational fluid dynamics (CFD) simulations were employed in conjunction with central composite design (CCD). The study took into account various geometric

parameters that affect the rotor's performance, including the number of blades ( $N$ ), helix angle ( $\gamma$ ), and aspect ratio ( $AR$ ). The focus was on maximizing the power coefficient to determine how each geometric factor influenced the GHT's efficiency. The numerical results obtained were validated experimentally using a hydraulic bench and a scale model of the GHT. This work provides valuable insight into improving the performance of the GHT and its potential application in hydrokinetic energy generation.

## 2. Materials and Methods

### 2.1. Gorlov Helical Turbine Fundamentals

The GHT is a unique design that features long helical blades that resemble a screw thread and run along an imaginary cylindrical surface of rotation [6,12,15]. This design has been shown to offer increased stability and efficiency compared to other vertical-axis hydrokinetic turbines. Figure 1 displays the various geometric factors involved in GHT design, including  $D$  and  $H$ , which represent the diameter and height of the turbine. These parameters play a critical role in the overall performance of the GHT and have been the subject of extensive research and optimization efforts.

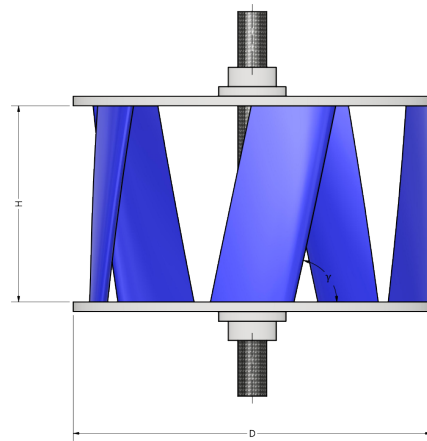


**Figure 1.** Geometric factors involved in the Gorlov helical turbine (GHT) design.

Equation (1) can be used to determine the amount of hydrokinetic power ( $P$ ) that a turbine is capable of generating based on its dimensions and the flow of water it receives [6,7].

$$P = \frac{1}{2} \rho A V^3 C_P \quad (1)$$

The variables  $\rho$  and  $V$  represent the density and free stream velocity of water, respectively.  $A$  denotes the swept area and is obtained by multiplying  $H$  and  $D$ .  $C_P$ , or the power coefficient, is a measure of how effectively a hydrokinetic turbine converts the kinetic energy of the water into electrical power. In this particular study, the values of  $P$ ,  $V$ , and  $\rho$  were set to 500 W, 1.5 m/s, and 997 kg/m<sup>3</sup>, respectively, and a design  $C_P$  of 0.3 was assumed. Once the swept area ( $A$ ) is determined,  $D$  and  $H$  can be calculated with the help of an aspect ratio ( $AR$ ), which is defined as the ratio of  $H$  to  $D$ . After reviewing the literature, it was found that NACA 0018, NACA 0020, and NACA 0022 hydrofoils are commonly used for the design of GHT blades [12,16–22]. To select the appropriate hydrofoil for this study, the JavaFoil 2.20 software was used to determine the hydrofoil with the highest ratio of lift coefficient ( $C_L$ ) to drag coefficient ( $C_D$ ) for the expected Reynolds number of the turbine operating conditions. The Reynolds number was calculated using Equation (2), and Table 1 shows the maximum  $C_L/C_D$  values obtained for the different hydrofoils studied.

$$Re = \frac{\rho V C}{\mu} \quad (2)$$

In the current study, the variables  $C$  and  $\mu$ , which represent the chord length and dynamic viscosity of water, respectively, were assumed to be 0.33 m and 0.001002 kg/ms [23]. As a result, the Reynolds number was calculated to be 492,529.94. The NACA 0018 hydrofoil demonstrated the best overall performance, making it the ideal choice for the design of the turbine blade. Its superior lift-to-drag ratio and low drag coefficient were critical factors that contributed to its selection for this application.

**Table 1.** Lift coefficients and drag ratios for evaluated hydrofoil.

Hydrofoil	Angle of Attack ( $\alpha$ )	$C_L/C_D$	$C_L$	$C_D$
NACA 0018	9.50	30.619	1.118	0.037
NACA 0020	9.75	29.885	1.161	0.039
NACA 0022	9.75	28.374	1.175	0.041

## 2.2. Response Surface Methodology Analysis

In this study, the impact of geometrical factors, specifically  $N$ ,  $\gamma$ , and  $AR$ , on the performance of GHT was investigated using RSM. The advantage of using this approach is that it allows for the examination of the effect of multiple factors and their interactions on the response variable, rather than assessing one factor at a time [24,25]. RSM helps to identify optimal design configurations that might otherwise be overlooked if each parameter were tested independently. Additionally, RSM allows for the development of predictive models, providing valuable insights into how changes in these factors impact overall performance, ultimately guiding the design and optimization process in a more efficient and systematic way. This leads to enhanced turbine efficiency and reliability, which is critical for maximizing energy extraction from water currents [24,25].

The performance of the turbine was evaluated by determining  $C_p$ , which can be obtained through Equation (3). To present the turbine performance, the  $C_p$  vs. TSR (tip speed ratio) curve is typically used. This curve is essential because it provides a clear visual representation of the turbine's performance across different flow conditions, offering insights into both efficiency and stability. For example, at low TSR values, the turbine may not be rotating fast enough to effectively harness the energy from the flow, resulting in low  $C_p$  values. On the other hand, at excessively high TSRs, the blades may rotate too quickly, creating more drag than useful power generation, which also reduces efficiency. The peak of the  $C_p$  vs. TSR curve indicates the optimal TSR at which the turbine achieves maximum power output, making this an invaluable tool for optimizing the turbine's design and operational settings. The TSR is defined as the ratio between the tangential speed of the blade tip and the upstream flow velocity, which can be calculated using Equation (4) [25].

$$C_p = \frac{T\omega}{\frac{1}{2}\rho AV^3} \quad (3)$$

$$\text{TSR} = \frac{R\omega}{V} \quad (4)$$

The variables  $T$ ,  $\omega$ , and  $R$  represent the turbine's torque, angular velocity, and radius, respectively. The levels of these factors were determined based on a literature review. Table 2 provides an overview of the values adopted for the geometric variables involved in the design of a GHT, both for hydrokinetic and wind power applications. The maximum efficiency achievable by this type of turbine is constrained by the Betz limit, which has a theoretical maximum of 0.5926 [25]. Various studies have reported that altering certain geometric parameters can enhance both the  $P$  and  $C_p$  of the GHT. Therefore, it is of interest to investigate the effects of these factors and their interactions using an appropriate methodology, such as RSM.

**Table 2.** Variables employed in the design and some research conducted on helical or Gorlov-type hydrokinetic turbines.

Reference	Type of Study	Height (H)	Diameter (D)	Helix Angle ( $\gamma$ )	Number of Blades (N)	Solidity ( $\sigma$ )	Hydrofoil	Aspect Ratio (AR)	Results Obtained	Additional Relevant Information
Talukdar et al. (2017) [16]	Experimental	0.25 m	0.25 m	43.7°	3	0.2	NACA0022	1	A higher efficiency is achieved for the single-pitch configuration, with a maximum $C_p$ of 0.16 and 0.14 obtained for the single-pitch and double-pitch configurations, respectively, at TSRs of 2.82 and 3.90.	A comparative study is conducted for two turbine configurations, single-pitch and double-pitch, which were investigated at inlet velocities of 1.3 m/s and 1.1 m/s, respectively.
Gorlov A. (2002) [12], Gorlov A. (1998) [17]	Analytical and experimental development	0.8636 m	0.6096 m	60°	3	0.27	NACA0020	1.4166	A power output of 2.4 kW was obtained for the turbine, with a maximum $C_p$ of 0.35 achieved for TSRs between 2.0 and 2.2.	Analysis of the helical or Gorlov turbine and its applications, the maximum velocity measured on site was 1.6764 m/s.
Dabbagh and Yuce (2019) [18]	Numerical	1.5 m	1 m	-	3	0.15, 0.2, 0.25, 0.3	NACA0018	1.5	For turbines with solidity ratios of 0.15 and 0.2, better efficiencies were obtained than for the other two cases. The maximum $C_p$ was 0.387, for a solidity ratio of 0.15 and a TSR of 2.	Numerical CFD analysis using the $k-\omega$ SST turbulence model under different flow conditions, for Reynolds numbers ranging from $5 \times 10^5$ to $2.5 \times 10^6$ .
Kirke (2011) [19]	Experimental	1.25 m	1 m	-	3	-	NACA0020	1.25	It was observed that implementing the diffuser increased the output power by a factor of 3. The $C_p$ increased from 0.11 (TSR = 1.1) to 0.36 (TSR = 1.6).	Experiments conducted with and without diffuser at the turbine inlet. The experiments were carried out for velocity ranges between 1 and 5 m/s.
Han et al. (2013) [20]	Experimental	Case 1: 2.5 m, Case 2: 3.6 m	Case 1: 2.2 m, Case 2: 3 m	Case 1: 65.3°, Case 2: 66.4°	3 (both cases)	-	NACA0020 (both cases)	Case 1: 1.1364, Case 2: 1.2	For case 2, a higher efficiency was obtained, with a $C_p$ of 0.329, while in case 1 a $C_p$ of 0.3 was obtained. The nominal power in both cases was 500 kW.	-
Bachant et al. (2011) [21]	Experimental	T <sub>1</sub> : 1.32 m, T <sub>2</sub> : 0.97 m	T <sub>1</sub> : 1 m, T <sub>2</sub> : 1.14 m	-	T <sub>1</sub> : 3, T <sub>2</sub> : 4	T <sub>1</sub> : 0.14, T <sub>2</sub> : 0.22	NACA0020 (both turbines)	T <sub>1</sub> : 1.32, T <sub>2</sub> : 0.851	Turbine T <sub>1</sub> is more effective than turbine T <sub>2</sub> , with a $C_p$ of 0.28 for T <sub>1</sub> and a $C_p$ of 0.21 for T <sub>2</sub> . The peak exergetic efficiency is higher for T <sub>1</sub> than for T <sub>2</sub> , with values of 46% and 35%, respectively.	Two turbines evaluated: T <sub>1</sub> (Gorlov-type) and T <sub>2</sub> (Spherical-type).
Talukdar et al. (2016) [16]	Numerical	-	-	-	-	-	NACA0018, NACA0022, NACA0015	-	NACA0022 airfoil exhibits better power output than NACA0018 and NACA0015 airfoils, with 12.24% and 22.47% higher power output for NACA0022.	Numerical study using CFD with a commercial URANS solver; and 3D transient simulations conducted.
Talukdar et al. (2015) [22]	Experimental	0.3 m	0.3 m	60°	3	0.38	NACA0020	1	The maximum $C_p$ obtained was 0.14 at a TSR of 1.01.	Experiments conducted at a water velocity of 0.8 m/s.

An investigation was performed to determine the optimal geometric configuration of the turbine for maximizing  $C_p$  based on the factors  $N$ ,  $\gamma$ , and  $AR$ . For each of these factors, three levels were defined: the maximum value, the minimum value, and the mean value reported in the literature. The specific values selected for each factor are presented in Table 3.

**Table 3.** Chosen values for the experimental design (DOE) variables.

Factor	Maximum Value	Minimum Value	Mean Value
Number of blades ( $N$ )	6 [26]	2 [27]	4
Helix angle ( $\gamma$ )	84.8° [28]	30.0° [29]	57.4°
Aspect ratio ( $AR$ )	1.5 [30]	0.5 [30]	1.0

Experimental design is essential in scientific research, enabling systematic hypothesis testing and optimization of processes. Various designs, such as full factorial, central composite design (CCD), Latin hypercube design (LHD), Box–Behnken, and Taguchi methods, offer distinct advantages depending on the study's complexity and goals. Among these, CCD is widely used for its efficiency, reducing experimental runs while still capturing both linear and quadratic effects. It strikes a balance between precision and workload by using factorial, axial, and center points, making it ideal for modeling complex systems. While CCD is particularly suited for optimization tasks, LHD offers an advantage in high-dimensional problems by evenly sampling the design space with fewer runs, making it useful for computational models. Box–Behnken designs provide efficiency in certain cases but may miss boundary conditions, and Taguchi methods focus on robustness and quality control but may overlook complex interactions. The number of experimental runs in CCD is determined based on the factors and center points, ensuring efficient exploration of the response surface. In this context, CCD stands out for its balance of flexibility, efficiency, and precision, while other designs serve well in specific contexts like high-dimensional exploration or early-stage screening [24]. In the context of CCD, a mathematical model is created to express the response variable as a function of the factors under investigation. The required number of experimental runs is influenced by both the number of factors being analyzed and the inclusion of center points within the experimental domain, which are necessary for estimating the variability in the measurements. The total number of runs can be calculated using the following Equation (5) [24,25,31]:

$$m = k^2 + 2k + n \quad (5)$$

where  $k$  represents the number of factors and  $n$  denotes the number of center points within the experimental domain. In the current study, a CCD was used to optimize a system consisting of three factors, with two replicates at the central point. Based on the above equation, the total number of runs needed for this optimization was determined to be 17. Table 4 presents the experimental matrix for the design of experiments (DOE).

Upon completion of 17 randomly conducted experiments, regression models were created using the data acquired from the simulations. The formulation described in Equation (6) depicts a comprehensive regression model that encompasses three independent variables ( $N$ ,  $\gamma$ , and  $AR$ ) and the dependent variable ( $C_p$ ). A second-order model was chosen over linear models because it offers a more accurate representation of complex interactions and non-linear behaviors often encountered in engineering problems. Unlike linear models, which only account for straightforward, additive relationships between variables, a second-order model incorporates quadratic terms that capture the curvature of the response surface. This allows it to better represent the non-linear effects and interactions between factors. In engineering applications, where systems frequently exhibit intricate and non-linear behaviors, a second-order model provides a more comprehensive understanding of how variables influence each other and the overall system performance. By including both linear and quadratic terms, the model can identify optimal conditions and predict outcomes with greater precision. This improved accuracy enhances the quality

of the experimental design and the reliability of the results, making it a crucial tool for effective process optimization and system design [25].

**Table 4.** Experimental matrix for the central composite design (CCD).

Run	Number of Blades (N)	Helix Angle ( $\gamma$ )	Aspect Ratio (AR)
1	2	84.8	0.5
2	4	57.4	1.0
3	2	30.0	0.5
4	6	57.4	1.0
5	6	30.0	1.5
6	2	57.4	1.0
7	6	84.8	0.5
8	4	57.4	0.5
9	4	57.4	1.0
10	2	30.0	1.5
11	4	84.8	1.0
12	4	30.0	1.0
13	6	30.0	0.5
14	4	57.4	1.5
15	2	84.8	1.5
16	6	84.8	1.5
17	4	57.4	1.0

$$C_p = \beta_0 + \beta_1 N + \beta_2 \gamma + \beta_3 AR + \beta_{12} N \cdot \gamma + \beta_{13} N \cdot AR + \beta_{23} \gamma \cdot AR + \beta_{11} N^2 + \beta_{22} \gamma^2 + \beta_{33} AR^2 \quad (6)$$

where  $\beta_0$  is the constant term and  $\beta_1$ ,  $\beta_2$ , and  $\beta_3$  are linear coefficients associated with the independent factors. The quadratic coefficients  $\beta_{11}$ ,  $\beta_{22}$ , and  $\beta_{33}$  capture the influence of the square of the independent variables on the dependent variable. The interaction effects of the independent variables on the dependent variable are represented by coefficients  $\beta_{12}$ ,  $\beta_{13}$ , and  $\beta_{23}$  [25].

The data obtained from the simulations were analyzed numerically using analysis of variance (ANOVA) to evaluate the significance of each model term. The contribution of each term was assessed through the  $p$ -value and F-ratio, with low  $p$ -values and high F-ratios indicating a significant impact. Coefficients with  $p$ -values below the predetermined significance threshold were considered to have statistically significant effects. Interactions between factors and the response variable were examined, leading to the identification of optimal values for the studied geometric parameters. To quantify the proportion of variability explained by the regression models, both the correlation coefficient ( $R^2$ ) and the adjusted determination coefficient ( $R_{adj}^2$ ) were computed. Additionally, the  $p$ -value of the regression models was determined to assess their reliability in capturing the experimental results. Three-dimensional (3D) plots were created to visualize the effects of design factors on the selected turbine's  $C_p$ . The statistical analysis was performed using the R-4.2.3 Project for Statistical Computing software, with a 95% confidence level [24,25].

### 2.3. Numerical Simulation

#### 2.3.1. Computational Domain and Meshing

To assess the impact of  $N$ ,  $\gamma$ , and  $AR$  on the performance of GHT, a series of computational fluid dynamics (CFD) studies were conducted using the Ansys Fluent software, version 2021R1. The study of computational domain independence is essential for ensuring the accuracy and reliability of numerical simulations in computational modeling. The size and configuration of the computational domain can directly affect the results; if the domain is too small, boundary effects may distort the system's physical behavior, while excessively large domains can unnecessarily increase computational costs. Therefore, analyzing domain independence helps identify the optimal domain size that guarantees accurate results without excessive resource consumption. In this study, four domain sizes (A, B, C, D) were examined, with their dimensions presented in Table 5. The computational domain is a complex system that is characterized by various factors that influence its behavior. One such factor is the use of fixed and rotating domains within a three-dimensional space. This do-

main consists of two separate subdomains: a fixed rectangular parallelepiped representing a water channel, and a cylindrical inner subdomain that houses the turbine [23].

**Table 5.** The computational domains studied.

Computational Domain	Width	Height	Upstream Distance	Downstream Distance	Diameter of the Rotational Domain
A	4D	3.33H	2D	4D	1.5D
B	8D	7H	4D	8D	1.5D
C	12D	10H	6D	14D	1.5D
D	16D	10H	8D	20D	1.5D

To study the independence of the computational domain, it is necessary to establish a control variable for comparative purposes between the different computational domains. In this case, the control variable selected is the  $C_p$  found for a given TSR. For comparative purposes between the three computational domains, a TSR of 1.5 was assumed. The values of the relative errors found for each computational domain with respect to the following one, going from the smallest to the largest computational domain, are presented in Table 6.

**Table 6.** Relative errors for each computational domain studied.

Computational Domain	Number of Elements	Control Variable $C_p$	Relative Error (%)
A	456,872	0.048	6.391
B	465,920	0.045	1.213
C	475,285	0.044	0.603
D	468,429	0.044	–

For the CFD analysis, domain C was selected as the computational domain, and its general dimensions are presented in Table 5. In addition, images of the selected computational domain, the boundary conditions, and the primary dimensions employed within the computational domain are shown in Figure 2. Domain C is suitable for the CFD analysis due to its specific features, including its size, shape, and complexity. The dimensions of domain C are within the acceptable range for the chosen computational model, and the shape of the domain is representative of the physical system being studied. Moreover, the complex features of the domain, such as the presence of multiple components and the interaction between them, provide a realistic representation of the real-world system. Overall, the selection of domain C for the CFD analysis is expected to provide accurate and reliable results that can inform the understanding of the physical system under study.

An inlet boundary condition was defined on the left side of the water channel, with a uniform velocity of 1.5 m/s and a turbulence intensity of 10%. The choice of 1.5 m/s was based on the fact that rivers in developing regions typically have flow velocities below 2 m/s and are not deep enough to accommodate large-diameter axial turbines [32,33]. On the right side, the outlet boundary condition was set with a relative pressure of 0 Pa, with the flow directed from  $-x$  to  $x$ . The remaining four boundaries were assigned free-slip wall conditions, while interface boundary conditions were applied between the cylindrical inner subdomain and the rectangular parallelepiped water channel to maintain fluid continuity and reduce simulation time. The rotor center was defined as the origin of the reference frame. The simulation started with the rotor at rest and without load, progressing until the axial turbine began rotating counterclockwise at a constant angular velocity ( $\omega$ ) around the  $+z$  axis.  $\omega$  was specified as a boundary condition for the rotational motion. The change in turbine  $\omega$  resulted in a change in the TSR and  $C_p$  values, enabling the evaluation of the turbine performance curve for the 17 configurations resulting from the selected DOE.

On the other hand, two of the factors that can also affect the accuracy of the results are the size of mesh and the time step used in the simulation. Therefore, it is essential to conduct an independence analysis of the mesh and the time step in order to evaluate their impact on the numerical results. Using the selected domain C, mesh densification methods were applied in the regions adjacent to the blade wall in all the conducted analyses.

These methods took into account the values for the laminar and turbulent boundary layer thicknesses, which were 2.33 mm and 9 mm, respectively, for the minimum distance “ $y$ ” that the first cell must have between the blades and the fluid, as previously described. Furthermore, the  $y^+$  criterion was considered, and a value of 0.015 was obtained. A growth factor of 1.2 was used for the layers following this until the turbulent layer was completely covered.

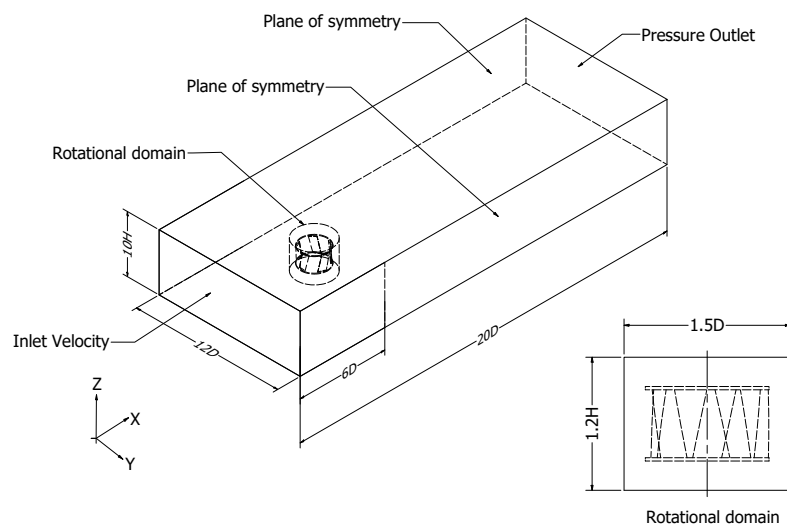


**Figure 2.** Dimensions of the computational domain and the setup of boundary conditions for the Ansys Fluent simulation.

For the mesh independence study, four different meshes were analyzed. The results of the mesh independence study are presented in Table 7. As can be observed, meshes with 923,945 elements yield independent and reliable results. Therefore, mesh C was selected for the simulations. Figure 3 shows the detailed mesh selected based on the conducted mesh independence study. Maintaining mesh quality metrics is essential to ensuring accurate and stable numerical simulations. Poor mesh quality can lead to errors in the results, convergence issues, and increased computational time, especially in areas with complex geometries or high gradients. Key parameters such as element quality, aspect ratio, skewness, and orthogonality must be carefully controlled to minimize distortions and ensure that the mesh accurately represents the physical domain. In this study, all relevant mesh quality metrics were preserved throughout the analysis, ensuring that the mesh was both robust and optimized for accurate simulation results, without introducing numerical errors.

**Table 7.** Relative errors for each mesh studied.

Computational Domain	Number of Elements	Control Variable $C_p$	Relative Error (%)
A	436,053	0.043	35.220
B	707,804	0.066	2.955
C	923,945	0.064	0.873
D	1,017,205	0.063	–

In this study, four different time step sizes were analyzed to determine their effect on the numerical results. The results of the analysis are presented in Table 8. By conducting this analysis, we can ensure that the numerical results obtained from the simulation are reliable and independent of the time step size used. In numerical simulations, a time step of 0.002728531 s was utilized, as it demonstrated result independence and provided a stable convergence.

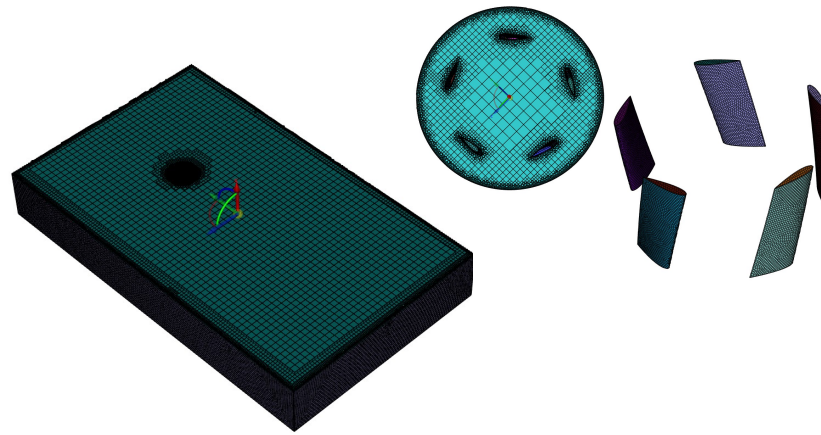


**Figure 3.** Mesh of computational domain dimensions.

**Table 8.** Relative errors for each time step studied.

Time Step	Value (s)	Control Variable $C_p$	Relative Error (%)
A	0.010914126	0.070	2.592
B	0.005457063	0.068	6.651
C	0.002728531	0.064	0.007
D	0.001364266	0.064	–

Once the computational domain, optimal mesh, and appropriate time step were established, 17 simulations were conducted to obtain the power coefficient for each combination of factors in the experimental design. The selection of an appropriate turbulence model is crucial for accurately simulating the flow behavior, particularly when dealing with adverse pressure gradients. In this study, the  $k-\omega$  SST turbulence model was chosen due to its capability to address such problems [25]. Additionally, it was ensured that the  $y^+$  values for the simulations were within the recommended range for this model. In this way, the simulations were able to capture the flow characteristics accurately and provide reliable results for the given problem. This approach highlights the importance of considering both the turbulence model selection and  $y^+$  values to improve the accuracy and reliability of simulations for complex fluid dynamics problems. Water was chosen as the fluid, and an aluminum alloy was chosen as the turbine material.  $C_p$  was obtained for various TSR values by setting the rotational speed of the rotor for the analyzed TSR. In the simulation stage, the Ansys Fluent software (version 2021R1) was used to apply the sliding mesh method. This is an advanced technique in computational fluid dynamics (CFD) used to model transient flows in rotating machinery such as turbines, fans, and pumps, where the interaction between rotating and stationary components is critical. Unlike other approaches, this method allows the mesh associated with the rotating component to physically move with the rotor, while the mesh in the stationary zone remains fixed. The interaction between these two meshes at the interface accurately simulates the flow, capturing the effects of rotation and relative motion in real time. This is essential for phenomena like vortex generation, flow separation, and pressure variations caused by the passing blades. Although the sliding mesh method provides higher accuracy in modeling transient effects, it requires a transient simulation with small time steps, making it computationally expensive. However, its ability to accurately capture complex fluid interactions in rotating machinery makes it invaluable for applications such as turbomachinery, propellers, and wind turbines, where the dynamic behavior of the flow is key to optimizing performance and preventing issues like cavitation or premature wear [34,35].

To configure the sliding mesh method in Ansys Fluent (version 2021R1), you must set up both the rotating and stationary domains accurately and apply an angular velocity to the rotating domain. First, in the geometry stage, define the regions for the rotating and stationary parts, such as the rotor (rotating zone) and stator (stationary zone). These domains must share an interface for fluid interaction. After defining the fluid domains,

proceed to mesh each domain separately, ensuring that the mesh at the interface between the rotating and stationary zones is well matched for smooth data transfer [34,35].

Once meshing is complete, set the boundary conditions by applying a moving reference frame to the rotating domain. In Ansys Fluent (version 2021R1), navigate to cell zone conditions for the rotating domain, and assign the rotation axis direction along with the desired rotational speed (in either RPM or rad/s). This step imposes the rotational motion on the sliding mesh. Afterward, create a mesh interface in Ansys Fluent (version 2021R1), which allows for the exchange of information such as velocity and pressure between the rotating and stationary zones [34,35].

It is crucial to configure the solver to transient mode, as the sliding mesh method requires capturing the dynamic interactions over time. Select an appropriate time step size, based on the rotational speed and the geometry, to ensure accurate representation of the transient effects. Finally, once the solution is obtained, you can analyze parameters such as torque, pressure distribution, and flow patterns in the post-processing stage to evaluate the performance of the rotating machinery. By properly configuring these parameters, the sliding mesh method will simulate the fluid interactions between rotating and stationary components with high physical accuracy. Therefore, to investigate the effect of rotational speed on the flow field,  $\omega$ , was varied from 0.5 rad/s to 6 rad/s in increments of 0.5 rad/s. By implementing the MRF method and varying the rotational speed, it was possible to accurately capture and analyze the flow behavior in the rotating machinery under investigation. To calculate  $C_p$ , the turbine was allowed to rotate for at least two revolutions to achieve stabilization. The  $C_p$  was computed using Equation (3) based on the numerical results from the last rotation. To accurately assess the performance of a Gorlov hydrokinetic turbine in CFD simulations, the approach typically involves running the simulation until the turbine completes at least two full revolutions to achieve stabilization. This method is necessary to ensure that the results reflect steady-state behavior, minimizing transient effects from initial conditions and allowing flow dynamics to develop fully around the blades. This setup is particularly crucial in hydrokinetic applications, where flow and pressure variations can significantly affect the turbine's performance coefficients, such as the  $C_p$  and torque measurements. Monitoring parameters like torque and  $C_p$  over successive revolutions ensures that any fluctuations settle within an acceptable range, indicating convergence to a quasi-steady state. Studies often apply similar convergence criteria to validate CFD models, especially for vertical-axis turbines. For instance, research on Gorlov and other helical turbines frequently examines torque stabilization to validate performance metrics across various flow conditions. These studies underscore the need for a dynamic mesh approach to capture changing flow patterns and to account for the effect of turbulence models (e.g.,  $k-\omega$  SST) on predictive accuracy [36,37].

### 2.3.2. Six-Degrees-of-Freedom (6DOF) Model

In CFD simulations of turbine rotation in Ansys Fluent, two key methodologies are commonly employed: the sliding mesh method and the six-degrees-of-freedom (6DOF) model. Each method is suited to different types of flow–structure interaction analysis and rotational dynamics [25,35,38].

The sliding mesh method is particularly effective for modeling the interaction between the flow and rotating blades in turbines, such as Gorlov or helical turbines. This method involves rotating an internal mesh while maintaining a fixed external mesh, simulating the continuous motion of the turbine blades within the flow field. At each time step, the interface between the rotating and stationary meshes is updated, enabling detailed monitoring of performance parameters such as the  $C_p$  and torque. However, this approach is computationally expensive due to the need to constantly update the mesh interface and the resolution required for accurate results. The sliding mesh method is most suitable for simulations where precision in capturing the cyclical dynamics of the turbine is crucial, particularly when studying performance metrics and flow interactions during steady rotational motion [38].

In contrast, the 6DOF model is used to simulate turbines where the motion is not entirely constrained, allowing for the turbine to move freely in space. This method is essential in applications such as hydrokinetic turbines, where external forces and varying flow conditions affect the turbine's motion in multiple axes. The 6DOF model captures not only the rotational motion of the turbine but also the translational movements caused by external forces and changing flow dynamics. While less efficient than the sliding mesh method for purely rotational simulations, the 6DOF model is valuable in scenarios where it is important to account for dynamic responses of the turbine structure to fluctuating flow conditions or environmental disturbances [15,38,39].

Both methods are integral for the accurate simulation and analysis of hydrokinetic turbines, and the selection of which to use depends on the specific objectives of the simulation. The sliding mesh method is preferred for high-precision analysis of rotational dynamics and flow interactions, whereas the 6DOF model is suited for studies requiring more complex dynamics, such as the response of turbines to varying flow patterns and external forces [38,39].

After obtaining the optimal configuration of GHT through RSM and CFD, a numerical analysis of a laboratory-scale GHT was performed to compare numerical and experimental results. For this, a three-dimensional computational domain in the Ansys Fluent software, version 2021R1, was utilized, along with the  $k\text{-}\omega$  SST turbulence model for unsteady flow simulations. The six-degrees-of-freedom (6DOF) user-defined function (UDF) method was used in the numerical simulation. Based on the simulations, the  $C_P$  versus TSR curve was plotted. This method allows for free movement in all translational and rotational axes, enabling a realistic representation of the interaction between the fluid and the rotating blades. By coupling fluid dynamics with the rigid body motion of the blades, 6DOF accounts for complex interactions that impact performance, such as aerodynamic drag, lift, and torque. This method is essential for optimizing turbine designs, as it provides insight into how varying fluid conditions and design parameters affect efficiency and structural loading. While the approach offers significant advantages in terms of precision and flexibility, it requires advanced programming with UDFs, increased computational resources, and can pose challenges in numerical stability. Nevertheless, its ability to simulate the turbine's real-time response to changing fluid forces makes it invaluable for performance prediction, design optimization, and fatigue analysis in energy applications [25,35].

The laboratory scale used was 1:7.53, with the dimensions of the scaled model defined to match the optimal turbine configuration (5 blades, an angle of inclination of  $78^\circ$ , and an aspect ratio of 0.6). The numerical simulations took into account the results of various independence studies conducted earlier, including domain independence, mesh independence, and time step independence. The inlet velocity defined at the computational domain was 0.6 m/s, the same velocity used in the experimental tests. The torque generated by the turbine was obtained through Ansys Fluent, version 2021R1, which implicitly solves Equation (7) [35].

$$T = J \frac{d\omega}{dt} \quad (7)$$

where  $J$  is the moment of inertia of the turbine. The rotation speed at time  $i + 1$  is obtained using Equation (8) [35].

$$\omega_{i+1} = \frac{\theta_{i+1} - \theta_i}{t_{i+1} - t_i} = \frac{\Delta\theta}{\Delta t} \quad (8)$$

where  $\theta$  is the angular position of the turbine. These values are obtained through the results reported in the dynamic mesh using the 6 DOF method. Simulations are performed for each time step and the above procedure is repeated until the turbine rotation speed reaches a constant value or fluctuates periodically around a constant value. Once the behavior of the turbine is determined, the mechanical power generated by the turbine for each time step of the simulations is obtained using Equation (9) [35].

$$P_T = T\bar{\omega} \quad (9)$$

where  $\bar{\omega}$  is the average rotational speed of the turbine during the period when it reaches a constant value or fluctuates periodically around a constant value. On the other hand, the power coefficient obtained for each time step of the simulations is obtained through Equation (3). The main parameters or specifications of the optimal Gorlov turbine necessary for conducting the respective CFD analysis with the coupling to the 6 DOF method are presented in Table 9.

**Table 9.** Specifications of the optimal Gorlov turbine for 6 DOF analysis.

Parameter	Value or Description
Material	ABS
Moment of inertia	$9.61 \times 10^{-4} \text{ Kg m}^2$
Initial center of mass	Centroid (coordinates x, y, z = 0, 0, 0)
Initial angular velocity	0 rad/s

#### 2.4. Experimental Setup

The optimal model of the GHT turbine was manufactured using 3D printing, in order to validate the numerical results. The optimization process of the GHT was conducted on a turbine with a height and outer diameter of 0.100 m and 0.185 m, respectively. The optimal model was fabricated using acrylonitrile butadiene styrene (ABS) through a fused deposition modeling (FDM) process, with careful optimization of the printing parameters to ensure the structural robustness and performance of the turbine. ABS was selected due to its superior mechanical properties, including higher impact resistance and thermal stability compared to PLA. The printing speed was set at 40–60 mm/s, a common range for ABS, ensuring precision and good interlayer adhesion. The nozzle temperature was maintained at 230–250 °C, which is ideal for ABS, providing sufficient flow and strong layer bonding. To prevent warping, the bed temperature was set at 90–110 °C, enhancing bed adhesion and reducing the risk of delamination. A fill density of 25% was chosen, striking a balance between structural integrity and weight, ensuring the blades could endure operational loads while remaining buoyant. The layer height was set to 0.2 mm to maintain a smooth surface finish, crucial for minimizing drag and improving hydrodynamic efficiency. Additionally, an enclosed printing environment was utilized to prevent material shrinkage and warping, which are common issues with ABS. The scale of the laboratory model was set at 1:7.53, with its dimensions specifically designed to correspond to the ideal configuration of the turbine, which includes five blades, an inclination angle of 78°, and an aspect ratio of 0.6 [40].

The investigation was carried out in an open hydraulic channel, which measured 0.31 m in width, 0.5 m in height, and 8 m in length. To determine the water velocity, a flow-meter (FlowWatch FW450, General Tools and Instruments, Secaucus, NJ, USA) with a velocity accuracy of  $\pm 0.01$  m/s was utilized. An axial flow pump, driven by a 14.9 kW electric motor, was employed to circulate water through the channel, achieving water velocities up to 1 m/s. Three different points upstream of the rotor were measured and averaged to obtain the water velocity. Figure 4 depicts an overview of the test facility.

The variables  $T$  and  $\omega$  were determined by utilizing a torque sensor (Futek-Model TR605, Irvine, CA, USA) with an encoder, which had an accuracy of 0.000110 Nm. Real-time data acquisition was accomplished by connecting the sensor to an intelligent digital display (IHH500 pro, Irvine, CA, USA), which monitored its performance. The sensor was positioned above the water surface.

In order to obtain torque readings at various TSRs, a braking system was employed at one end of the torque sensor. The system incorporates a direct current (DC) motor and reverse current braking method, which involves using an electric motor as a brake in the turbine model. This method maintains the constant TSR of the turbine model. The DC motor is energized in the opposite direction to the turbine rotation, creating a reactive

torque that reduces the turbine's angular velocity ( $\omega$ ). The electric motor also functions as a generator that is slowed down by the power demanded by the system. The braking torque is regulated by pulse-width modulation (PWM), which adjusts the current flow to the DC motor. This is achieved using a microcontroller and power coupling circuit that link the microcontroller's signal to the DC motor's power supply. To decrease or increase the turbine's  $\omega$ , the microcontroller adjusts the PWM's duty cycle, thereby increasing or decreasing the energy received by the motor and the resultant braking torque [41].

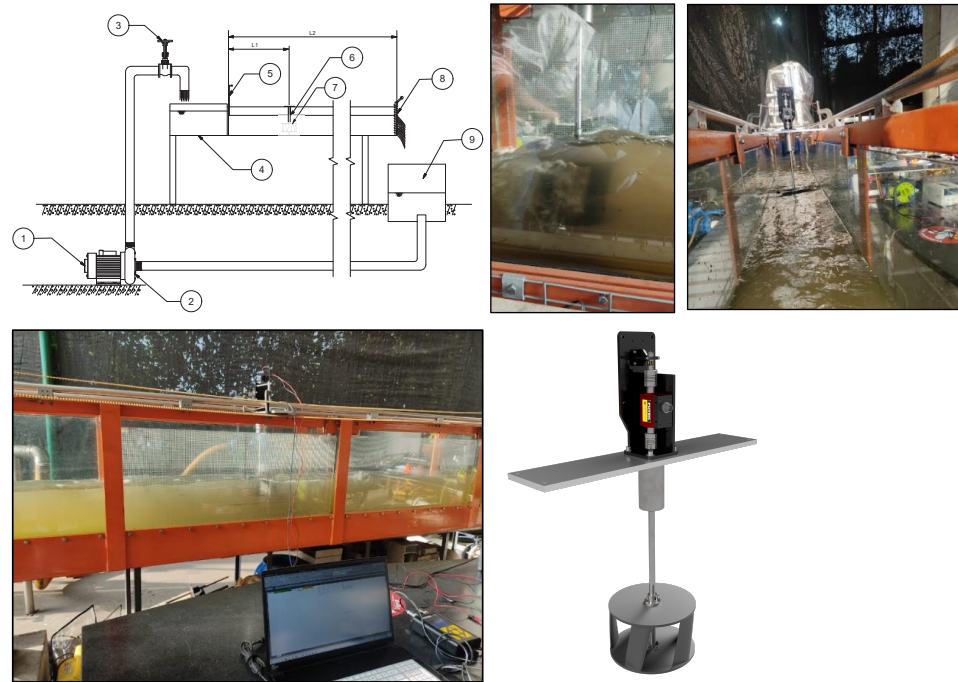


**Figure 4.** Experimental setup of the recirculating water channel. (1) Motor of 14.9 kW, (2) impeller, (3) water inlet valve, (4) channel, (5) gate, (6) model vertical-axis hydrokinetic turbine, (7) connection axis to the sensor, (8) weir assembly, and (9) feed tank.

In order to determine the non-dimensional power performance curve relating  $C_P$  to TSR, a uniform and steady flow was applied to the turbine model with the rotor positioned perpendicular to the flow direction.  $C_P$  values were obtained using Equation (3). The water's free stream velocity was kept constant at approximately 0.5 m/s, and the value of  $\omega$  was adjusted to generate various TSR values.

The blockage ratio ( $B_R$ ) is determined as the ratio of the projected area of the turbine to the cross-sectional area of the test section. According to the definition of  $B_R$ , when its value exceeds 10%, the effects of wall proximity become significant and must be considered, as they can substantially alter the flow dynamics around the turbine [42]. In this study, the projected turbine area is calculated as  $0.1 \text{ m} \times 0.185 \text{ m} = 0.0185 \text{ m}^2$ , and the test section area is  $0.31 \text{ m} \times 0.5 \text{ m} = 0.155 \text{ m}^2$ . This results in a  $B_R$  value of 11.935%, indicating that the blockage effect is non-negligible and necessitates the application of a correction procedure.

To account for the blockage effect, the method proposed by Pope and Harper [43,44] can be applied. This method corrects the flow velocity by multiplying the input velocity ( $V$ ) by a correction factor; therefore, the corrected velocity,  $V_c$ , is expressed as Equation (10) [43,44].

$$V_c = V \left( 1 + \frac{1}{4} B_R \right) \quad (10)$$

This corrected velocity can then be used to estimate the available energy and consequently  $C_P$  of the turbine. Given that the  $B_R$  in this study is only slightly above the 10% threshold, the impact of the blockage correction was considered minimal and therefore was not applied in this case.

### 3. Results and Discussions

The  $C_p$  for each treatment is presented in Table 10. These values were employed to conduct a statistical analysis of the chosen DOE.

**Table 10.** Central composite design (CCD) design matrix. Experimental and predicted responses for regression models.

Run	N	Factors $\gamma$	AR	Maximum Power Coefficient		TSR
				CFD Results ( $C_{P_{Max}}$ )	Predicted Results ( $C_{P_{Max}}$ )	
1	2	84.8	0.5	0.259	0.261	2.3
2	4	57.4	1.0	0.260	0.256	2.3
3	2	30.0	0.5	0.196	0.177	2.3
4	6	57.4	1.0	0.223	0.194	2.1
5	6	30.0	1.5	0.211	0.212	2.3
6	2	57.4	1.0	0.117	0.136	2.3
7	6	84.8	0.5	0.264	0.267	1.6
8	4	57.4	0.5	0.284	0.313	2.2
9	4	57.4	1.0	0.260	0.256	2.3
10	2	30.0	1.5	0.101	0.102	2.3
11	4	84.8	1.0	0.298	0.275	2.3
12	4	30.0	1.0	0.266	0.281	2.3
13	6	30.0	0.5	0.269	0.273	1.9
14	4	57.4	1.5	0.203	0.199	2.3
15	2	84.8	1.5	0.095	0.094	2.3
16	6	84.8	1.5	0.092	0.114	1.6
17	4	57.4	1.0	0.260	0.256	2.3

After conducting tests in a randomized order, an ANOVA analysis was carried out, and the findings are presented in Table 11. The results indicate that the terms N, AR, the quadratic effect  $N^2$ , and the interactions between N and  $\gamma$  and  $\gamma$  and AR have the lowest  $p$ -values. The other terms had insignificant influence on the response variable considering a significance level of 5%; i.e.,  $\gamma$ ,  $AR^2$ ,  $\gamma^2$ , and  $N \times AR$  did not have a significant effect on the  $C_p$  of the GHT.

**Table 11.** ANOVA for the regression model.

Factor	Sum of Squares (SS)	Degrees of Freedom (DOF)	Mean Sum of Squares (MS)	F-Ratio	$p$ -Value
N	$8.430 \times 10^{-3}$	1	$8.430 \times 10^{-3}$	17.552	0.004
$\gamma$	$1.300 \times 10^{-4}$	1	$1.300 \times 10^{-4}$	0.274	0.617
AR	$3.250 \times 10^{-2}$	1	$3.250 \times 10^{-2}$	67.650	$7.630 \times 10^{-5}$
$N^2$	$2.593 \times 10^{-2}$	1	$2.593 \times 10^{-2}$	53.982	$1.560 \times 10^{-4}$
$\gamma^2$	$1.470 \times 10^{-3}$	1	$1.470 \times 10^{-3}$	3.061	0.124
$AR^2$	$4.000 \times 10^{-4}$	1	$4.000 \times 10^{-4}$	0.831	0.392
$N\gamma$	$4.030 \times 10^{-3}$	1	$4.030 \times 10^{-3}$	8.392	0.023
NAR	$1.100 \times 10^{-4}$	1	$1.100 \times 10^{-4}$	0.221	0.653
$\gamma AR$	$4.230 \times 10^{-3}$	1	$4.230 \times 10^{-3}$	8.802	0.021
Residuals	$3.360 \times 10^{-3}$	7	0.00048	–	–

Subsequently, the regression model was constructed. The equation ascribed to the quadratic regression model is expressed by Equation (11). The term  $AR^2$  was not included in Equation (11) because it presents a  $p$ -value higher than the level of significance, therefore it was removed from the model. The model resulted in a high R (95.83%) and  $R_{adj}^2$  (90.46%), and a  $p$ -value lower than 0.05 ( $p$ -value of 0.0004926). Therefore, the quadratic regression model resulted in a highly significant model, representing the maximum  $C_p$  of the GHT of interest.

$$\begin{aligned}
 C_p = & -0.1227 + 0.2158N - 0.0001852\gamma - 0.03226AR \\
 & - 0.02267N^2 + 0.0000294\gamma^2 - 0.0004097N\gamma \\
 & + 0.003641NAR - 0.001678\gamma AR
 \end{aligned}
 \tag{11}$$

Afterwards, the maximum  $C_p$  was calculated as 0.3072 when  $N$ ,  $\gamma$ , and AR were equal to 5,  $78^\circ$ , and 0.6, respectively. The response surface plots obtained are illustrated in Figure 5.

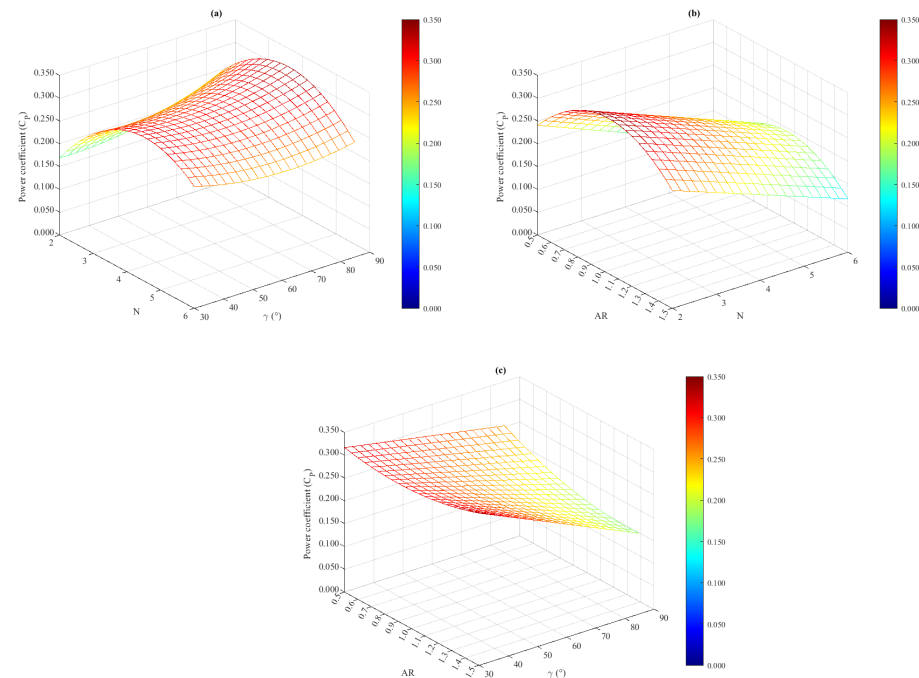


**Figure 5.** Response surface plots for the power coefficient ( $C_p$ ) by using the regression model. (a) Effects of  $N$  and  $\gamma$ ; (b) effects of  $N$  and AR; (c) effects of  $\gamma$  and AR. The other factors were set at the optimal values.

The performance of a GHT is intricately linked to several critical design factors,  $N$ , AR, and  $\gamma$ . The number of blades influences the turbine's energy capture efficiency: more blades can increase the amount of energy harvested from the water flow but may also introduce additional drag if not optimally balanced. This balance is essential because excessive drag can counteract the benefits of having more blades. The aspect ratio affects both the aerodynamic efficiency and the structural integrity of the blades. A higher aspect ratio generally improves energy extraction by allowing the blades to interact more effectively with the flow, but it can also make them more prone to mechanical stresses and bending. Conversely, a lower aspect ratio provides greater structural stability but may increase drag, potentially reducing overall efficiency. The helix angle, which describes the twist of the blades around the turbine axis, is crucial for optimizing how the blades interact with the water flow. An appropriately chosen helix angle ensures that the blades cut through the water smoothly, minimizing turbulence and drag. The interaction between the number of blades and the helix angle is particularly important; for instance, with a higher number of blades, the helix angle must be carefully tuned to avoid inefficient turbulence and ensure that each blade operates effectively. Additionally, the relationship between aspect ratio and helix angle must be optimized to ensure that longer, thinner blades do not experience excessive drag or structural issues. By meticulously adjusting these parameters and their interactions, the turbine can achieve a high  $C_p$ , ensuring maximum efficiency in converting the kinetic energy of the water flow into mechanical energy. Understanding and optimizing these design factors are therefore essential for maximizing the performance and efficiency of Gorlov-type hydrokinetic turbines.

In order to assess the suitability of the regression model constructed for representing the experimental data, it is necessary to verify several assumptions such as normality, residual independence, and homoscedasticity [25]. Normality can be evaluated using graphical

methods such as a normal probability plot and a histogram or frequency distribution plot. In this study, a frequency distribution plot (Figure 6a) and normal probability plot (Figure 6b) were generated to assess the normality of  $C_p$ . It was observed that the residuals did not perfectly align with the red lines depicted in Figure 6a,b. Therefore, numerical tests were performed to confirm if the experimental data were normally distributed. Several tests were carried out including the Kolmogorov–Smirnov (0.05971), Shapiro–Francia (0.1174), Shapiro–Wilk (0.0898), Jarque–Bera (0.7558), and D’Agostino and Pearson (0.7975) tests, all at a significance level of 5% [45]. The  $p$ -value associated with each test is shown in parentheses. As the  $p$ -values for all the normality tests conducted were greater than 0.05, it can be concluded that  $C_p$  follows a normal distribution.

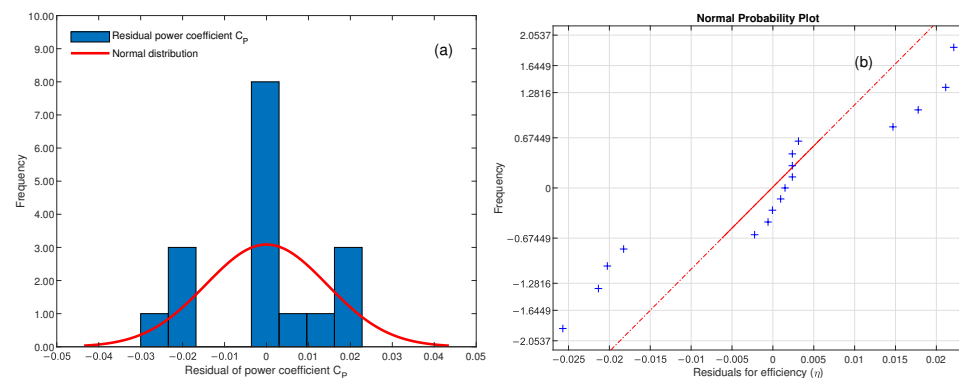


**Figure 6.** (a) Frequency distribution and (b) normal probability plots for the power coefficient ( $C_p$ ).

In addition to normality analysis, residual independence and homoscedasticity were checked. The Durbin–Watson test, as described by Albertson et al. [25,46], was used to test for residual independence, yielding a  $p$ -value of 0.914, indicating that the assumption of residual independence was satisfied. To assess homoscedasticity, we used the studentized Breusch–Pagan test and obtained a  $p$ -value of 0.7042, suggesting the presence of homoscedasticity. However, since the  $p$ -value was very close to the significance level, we lacked sufficient evidence to conclude that the response variable satisfied the assumption of homoscedasticity.

The results obtained for the  $C_p$  from the CFD simulations using the 6DOF methodology and the experimental data were plotted versus the tip speed ratio (TSR), whose value for each time step can be obtained using Equation (4). These values are reported in Figure 7. The comparison between simulation results and experimental data is crucial for validating the CFD model, as it helps in assessing the accuracy of the simulated turbine performance under dynamic operating conditions. In several studies, similar methodologies have been used to compare power coefficient curves, where the results from dynamic simulations often show good agreement with experimental data when the right convergence criteria and modeling techniques, such as 6DOF, are employed [25,35]. The standard deviation of the experimental data fluctuated between 3% and 5%. This range indicates a reasonable level of variability inherent in the measurements, reflecting the precision and consistency of the experimental process.

As can be observed, the power coefficient of the optimal GHT exhibits an increasing behavior as the TSR increases, then reaches its maximum value of 0.2868 for a TSR of 0.6837. The experimental results obtained from testing the scaled model in the hydraulic channel are also presented in Figure 7. Overall, the numerical and experimental results show a good correlation. The numerical results obtained for the scale model regarding the maximum power coefficient show a relative error of 4.302%. The differences may be attributed to the surface finish of the printed blades, which results from the printing process, as well as the quality of the surface roughness, which was not taken into account during the numerical simulation [47]. The influence of surface roughness on turbine performance becomes more pronounced as blade dimensions decrease, leading to an increase in relative roughness. In simulations, the blades are modeled as smooth surfaces without roughness, allowing

for unobstructed fluid flow and the resulting  $C_p$  values at the specified rotational speed. However, in experimental setups, surface roughness creates resistance to fluid flow due to fluid viscosity. As a result, to achieve the same relative velocity at the blade sections, equivalent forces must be applied, requiring the rotor to operate at higher speeds.

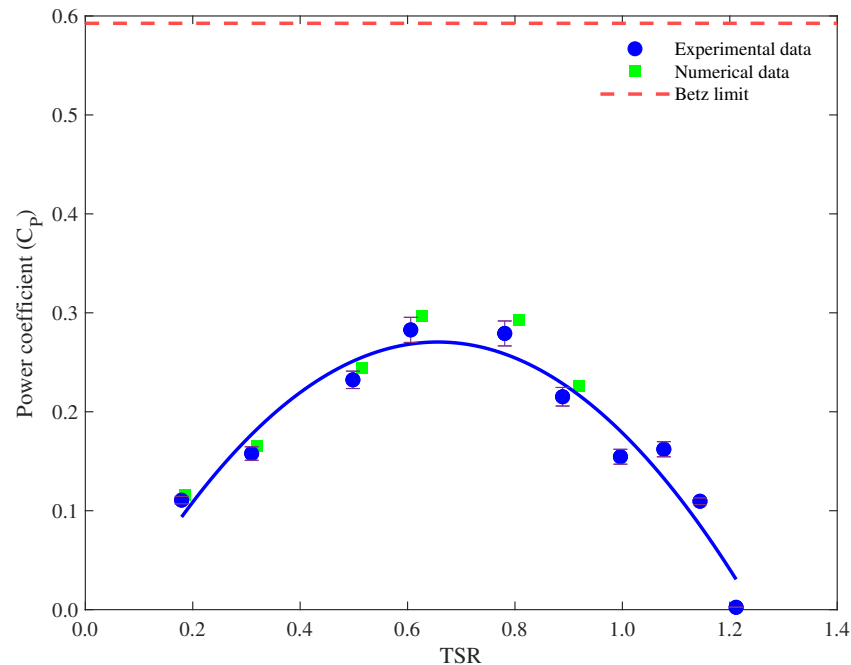


**Figure 7.** Numerical and experimental comparison of the power coefficient ( $C_p$ ) vs. tip speed ratio ( $\lambda$ ) curves.

From a technical standpoint, high flow rates are fundamental to the performance of Gorlov turbines. Increased flow velocities lead to higher rotational speeds, thereby maximizing the kinetic energy harnessed from the fluid. However, high flow rates also introduce complex flow dynamics, including turbulent eddies and variations in local flow velocity, which can impact turbine efficiency and longevity. Consequently, future work should focus on optimizing turbine performance under varying flow conditions to assess efficiency over a range of flow rates, particularly in environments with fluctuating flow characteristics.

On the other hand, the dynamic adaptation of the blade presents an intriguing avenue for enhancing efficiency. This adaptation could involve designing blades capable of adjusting their angle in real time to maintain an optimal angle of attack, thereby reducing drag and maximizing lift as flow conditions change. Implementing adaptive or flexible blades could improve performance in both high- and low-flow scenarios, although further investigation is needed to identify suitable materials and control systems capable of handling the stresses of continuous adjustment.

Moreover, while the current study did not explore new materials extensively, advancements in material science offer potential benefits for turbine performance. Using lightweight, corrosion-resistant composites could increase the turbine's lifespan and reduce maintenance requirements, particularly under high-stress conditions. Therefore, future research could investigate materials with enhanced fatigue resistance, as well as self-healing or bio-inspired materials, to mitigate wear in continuous, high-stress applications.

Finally, another crucial area for future study is the environmental impact of Gorlov turbines. Unlike propellers, which often operate in high-stress zones with significant risks of cavitation, Gorlov turbines may introduce different environmental effects due to their unique design and flow interaction. Key considerations include potential impacts on aquatic ecosystems, sediment transport, and flow patterns in natural water bodies. Thus, future research could explore the ecological compatibility of Gorlov turbines, assessing

both direct impacts on local aquatic life and broader environmental consequences, such as their influence on sediment dynamics and water quality. Addressing these aspects could pave the way for sustainable turbine designs that balance high energy output with minimal ecological disruption.

#### 4. Conclusions

Optimizing the design of the GHT rotor is a critical factor for reducing the cost of energy transformation in hydrokinetic systems. In this study, a numerical simulation was used to evaluate the optimization of the GHT rotor through the CFD method and the RSM. A regression model, was developed to relate the response variable ( $C_p$ ) to the factors of  $N$ ,  $\gamma$ , and AR. An ANOVA was conducted to determine the significance of the design variables on the GHT performance. The results showed that the factors  $N$ , AR, the quadratic effect  $N^2$ , and the interactions between  $N$  and  $\gamma$  and  $\gamma$  and AR significantly influenced the GHT performance. This study highlights the critical influence of blade number, aspect ratio, and helix angle on the performance of a Gorlov-type hydrokinetic turbine. The interaction between these factors is equally important, as a well-balanced combination can minimize drag, turbulence, and structural stress, maximizing the turbine's power coefficient ( $C_p$ ) and overall efficiency. The highest  $C_p$  values were obtained for  $N$ ,  $\gamma$ , and AR equal to 5,  $78^\circ$  and 0.6, respectively. The RSM and the second-order regression model are recommended for an optimal GHT design due to its high potential in power generation, ease of manufacture, installation, and good performance.

Future research on Gorlov-type hydrokinetic turbines should focus on several key areas to enhance their performance and adaptability. One important direction is the exploration of optimal blade designs that can dynamically adjust to varying flow conditions, such as changes in velocity or water depth, to improve energy capture efficiency. Additionally, the development of new materials that offer greater strength, durability, and flexibility will be crucial in creating blades that can withstand harsh environmental conditions without sacrificing performance. Furthermore, real-time control systems that can adjust turbine speed or blade orientation based on flow variations should be explored to optimize performance continuously. Finally, in-depth studies on the environmental impact of these turbines, including effects on aquatic ecosystems, will be vital to ensure sustainable deployment in diverse water resources.

**Author Contributions:** Conceptualization, J.C.P., A.R.-C. and E.C.; methodology, J.C.P., A.R.-C. and E.C.; software, J.C.P.; validation, J.C.P.; formal analysis, J.C.P., A.R.-C. and E.C.; writing—original draft, J.C.P., A.R.-C. and E.C.; writing—review and editing, A.R.-C. and E.C.; supervision, E.C.; project administration, A.R.-C. and E.C.; funding acquisition, E.C. All authors read and agreed to the published version of this manuscript.

**Funding:** The authors gratefully acknowledge the financial support provided by the Colombian Ministry of Science, Technology, and Innovation “MinCiencias” through “Patrimonio Autónomo Fondo Nacional de Financiamiento para la Ciencia, la Tecnología y la Innovación, Francisco José de Caldas” (Perseo Alliance, Contract No. 112721-392-2023)

**Data Availability Statement:** The original contributions presented in the study are included in the article, further inquiries can be directed to the corresponding author.

**Conflicts of Interest:** The authors declare that they have no conflicts of interest that could potentially influence the findings presented in this work.

#### References

1. Chien, F.; Huang, L.; Zhao, W. The influence of sustainable energy demands on energy efficiency: Evidence from China. *J. Innov. Knowl.* **2023**, *8*, 100298. [[CrossRef](#)]
2. Shang, Y.; Han, D.; Gozgor, G.; Mahalik, M.K.; Sahoo, B.K. The impact of climate policy uncertainty on renewable and non-renewable energy demand in the United States. *Renew. Energy* **2022**, *197*, 654–667. [[CrossRef](#)]
3. Holechek, J.L.; Geli, H.M.; Sawalhah, M.N.; Valdez, R. A global assessment: can renewable energy replace fossil fuels by 2050? *Sustainability* **2022**, *14*, 4792. [[CrossRef](#)]

4. Hassan, Q.; Viktor, P.; Al-Musawi, T.J.; Ali, B.M.; Algburi, S.; Alzoubi, H.M.; Al-Jiboory, A.K.; Sameen, A.Z.; Salman, H.M.; Jaszczur, M. The renewable energy role in the global energy Transformations. *Renew. Energy Focus* **2024**, *48*, 100545. [[CrossRef](#)]
5. Chaudhari, V.N.; Shah, S.P. Numerical investigation on the performance of an innovative Airfoil-Bladed Savonius Hydrokinetic Turbine (ABSHKT) with deflector. *Int. J. Thermofluids* **2023**, *17*, 100279. [[CrossRef](#)]
6. Reddy, K.B.; Bhosale, A.C.; Saini, R. Performance parameters of lift-based vertical axis hydrokinetic turbines-A review. *Ocean. Eng.* **2022**, *266*, 113089. [[CrossRef](#)]
7. Kumar, R.; Sarkar, S. Effect of design parameters on the performance of helical Darrieus hydrokinetic turbines. *Renew. Sustain. Energy Rev.* **2022**, *162*, 112431. [[CrossRef](#)]
8. Kishore, T.S.; Patro, E.R.; Harish, V.; Haghighi, A.T. A comprehensive study on the recent progress and trends in development of small hydropower projects. *Energies* **2021**, *14*, 2882. [[CrossRef](#)]
9. Elbatran, A.; Yaakob, O.; Ahmed, Y.M.; Shabara, H. Operation, performance and economic analysis of low head micro-hydropower turbines for rural and remote areas: A review. *Renew. Sustain. Energy Rev.* **2015**, *43*, 40–50. [[CrossRef](#)]
10. Khan, R.; Kumar, A. Performance enhancement of hydrokinetic turbine using augmentation techniques: a review. *Int. J. Green Energy* **2024**, *21*, 1667–1694. [[CrossRef](#)]
11. Osama, S.; Emam, M.; Ookawara, S.; Ahmed, M. Enhancing the performance of vertical axis hydrokinetic Savonius turbines using a novel cambered hydrofoil profile for rotor blades. *Ocean. Eng.* **2024**, *292*, 116561. [[CrossRef](#)]
12. Gorlov, A.M. The helical turbine and its applications for hydropower without dams. In Proceedings of the ASME International Mechanical Engineering Congress and Exposition, New Orleans, LA, USA, 17–22 November 2002; Volume 36266, pp. 257–264.
13. Etemadeasl, V.; Esmaelnajad, R.; Gharlai, K.; Riasi, A. Application of Entropy Production Theory for Evaluating the Performance of a Gorlov Hydrokinetic Turbine. *Iran. J. Sci. Technol. Trans. Mech. Eng.* **2024**, 1–20. [[CrossRef](#)]
14. Jayaram, V.; Bavanish, B. Design and analysis of gorlov helical hydro turbine on index of revolution. *Int. J. Hydrogen Energy* **2022**, *47*, 32804–32821. [[CrossRef](#)]
15. Chalaca, A.; Velásquez, L.; Rubio-Clemente, A.; Chica, E. Design and Optimization of a Gorlov-Type Hydrokinetic Turbine Array for Energy Generation Using Response Surface Methodology. *Energies* **2024**, *17*, 4870. [[CrossRef](#)]
16. Talukdar, P.K.; Kulkarni, V.; Das, A.K.; Dwivedy, S.K.; Kakoty, S.K.; Mahanta, P.; Saha, U.K. In-situ experiments to estimate the performance characteristics of a double-step helical-bladed hydrokinetic turbine. In Proceedings of the Gas Turbine India Conference, American Society of Mechanical Engineers, Bangalore, India, 7–8 December 2017; Volume 58516, p. V002T06A004.
17. Gorlov, A. Development of the helical reaction hydraulic turbine. In *Final Technical Report, 1 July 1996–30 June 1998*; Technical Report; Northeastern University: Boston, MA, USA, 1998.
18. Al-Dabbagh, M.; Yuce, M. Numerical evaluation of helical hydrokinetic turbines with different solidities under different flow conditions. *Int. J. Environ. Sci. Technol.* **2019**, *16*, 4001–4012. [[CrossRef](#)]
19. Kirke, B. Tests on ducted and bare helical and straight blade Darrieus hydrokinetic turbines. *Renew. Energy* **2011**, *36*, 3013–3022. [[CrossRef](#)]
20. Han, S.H.; Park, J.S.; Lee, K.S.; Park, W.S.; Yi, J.H. Evaluation of vertical axis turbine characteristics for tidal current power plant based on in situ experiment. *Ocean. Eng.* **2013**, *65*, 83–89. [[CrossRef](#)]
21. Bachant, P.; Wosnik, M. Performance measurements of cylindrical-and spherical-helical cross-flow marine hydrokinetic turbines, with estimates of exergy efficiency. *Renew. Energy* **2015**, *74*, 318–325. [[CrossRef](#)]
22. Talukdar, P.K.; Kumar, S.; Kulkarni, V.; Das, A.K.; Saha, U.K. On site testing of a zero head vertical axis helical water turbine for power generation. In *Proceedings of the Gas Turbine India Conference*; American Society of Mechanical Engineers: New York, NY, USA, 2015; Volume 57311, p. V001T11A001.
23. Arrieta, E.L.C.; Clemente, A.R. *Computational Fluid Dynamic Simulation of Vertical Axis Hydrokinetic Turbines*; IntechOpen: London, UK, 2019.
24. Montgomery, D.C. *Introduction to Statistical Quality Control*; John Wiley & Sons: Hoboken, NJ, USA, 2019.
25. Bouvant, M.; Betancour, J.; Velásquez, L.; Rubio-Clemente, A.; Chica, E. Design optimization of an Archimedes screw turbine for hydrokinetic applications using the response surface methodology. *Renew. Energy* **2021**, *172*, 941–954. [[CrossRef](#)]
26. Zamora Zapata, M.N. *Análisis Fluidodinámico en una Turbina Helicoidal GHT para Generación de Energía Mareo-Motriz*; Universidad de Chile: Santiago de Chile, Chile, 2012.
27. Gorlov, A. *Helical Turbine and Fish Safety*; Mechanical Engineering Department Northeastern University: Boston, MA, USA, 2010.
28. Marsh, P.; Ranmuthugala, D.; Penesis, I.; Thomas, G. Numerical investigation of the influence of blade helicity on the performance characteristics of vertical axis tidal turbines. *Renew. Energy* **2015**, *81*, 926–935. [[CrossRef](#)]
29. Pongduang, S.; Kayankannavee, C.; Tiaple, Y. Experimental investigation of helical tidal turbine characteristics with different twists. *Energy Procedia* **2015**, *79*, 409–414. [[CrossRef](#)]
30. Khan, M.; Iqbal, M.; Quaicoe, J. Design considerations of a straight bladed Darrieus rotor for river current turbines. In Proceedings of the 2006 IEEE International Symposium on Industrial Electronics, Montreal, QC, Canada, 9–13 July 2006; Volume 3, pp. 1750–1755.
31. Montgomery, D.C.; Peck, E.A.; Vining, G.G. *Introduction to Linear Regression Analysis*; John Wiley & Sons: Hoboken, NJ, USA, 2021.
32. Andreadis, K.M.; Schumann, G.J.P.; Pavelsky, T. A simple global river bankfull width and depth database. *Water Resour. Res.* **2013**, *49*, 7164–7168. [[CrossRef](#)]
33. Kirke, B. Hydrokinetic and ultra-low head turbines in rivers: A reality check. *Energy Sustain. Dev.* **2019**, *52*, 1–10. [[CrossRef](#)]

34. Szlivka, F.; Hetyei, C.; Fekete, G.; Molnár, I. Comparison of Mixing Plane, Frozen Rotor, and Sliding Mesh Methods on a Counter-Rotating Dual-Rotor Wind Turbine. *Appl. Sci.* **2023**, *13*, 8982. [[CrossRef](#)]
35. Betancour, J.; Velásquez, L.; Rubio Clemente, A.; Chica, E. Performance simulation of water turbines by using 6-DoF UDF and sliding mesh methods. *J. Appl. Res. Technol.* **2023**, *21*, 181–195.
36. Karakaya, D.; Bor, A.; Elçi, S. Numerical Analysis of Three Vertical Axis Turbine Designs for Improved Water Energy Efficiency. *Energies* **2024**, *17*, 1398. [[CrossRef](#)]
37. Rendi, R.; Arifin, J.; Pauzan, M. Enhanced Performance of the Gorlov Hydrokinetic Turbine through Blade Profile Modification. *SINTEK JURNAL J. Ilm. Tek. Mesin* **2024**, *18*, 19–25.
38. Mohammed, M.; Sarip, S.; Mustafa, W.A. Systematic Review of Computational Fluid Dynamics Modelling and Simulation Techniques Employed in Vertical Axis Hydrokinetic Turbines. *J. Adv. Res. Appl. Mech.* **2024**, *117*, 51–71. [[CrossRef](#)]
39. Betancour, J.; Romero-Menco, F.; Velásquez, L.; Rubio-Clemente, A.; Chica, E. Design and optimization of a runner for a gravitational vortex turbine using the response surface methodology and experimental tests. *Renew. Energy* **2023**, *210*, 306–320. [[CrossRef](#)]
40. Mendenhall, R.; Eslami, B. Experimental investigation on effect of temperature on FDM 3D printing polymers: ABS, PETG, and PLA. *Appl. Sci.* **2023**, *13*, 11503. [[CrossRef](#)]
41. Obando Vega, F.; Rubio-Clemente, A.; Chica, E. Control System for the Performance Analysis of Turbines at Laboratory Scale. *Energies* **2024**, *17*, 4950. [[CrossRef](#)]
42. Ryi, J.; Rhee, W.; Hwang, U.C.; Choi, J.S. Blockage effect correction for a scaled wind turbine rotor by using wind tunnel test data. *Renew. Energy* **2015**, *79*, 227–235. [[CrossRef](#)]
43. Jeong, H.; Lee, S.; Kwon, S.D. Blockage corrections for wind tunnel tests conducted on a Darrieus wind turbine. *J. Wind. Eng. Ind. Aerodyn.* **2018**, *179*, 229–239. [[CrossRef](#)]
44. Zhang, D.; Guo, P.; Cheng, Y.; Hu, Q.; Li, J. Analysis of blockage correction methods for high-solidity hydrokinetic turbines: Experimental and numerical investigations. *Ocean. Eng.* **2023**, *283*, 115185. [[CrossRef](#)]
45. Gallego, E.; Rubio-Clemente, A.; Pineda, J.; Velásquez, L.; Chica, E. Experimental analysis on the performance of a pico-hydro Turgo turbine. *J. King Saud Univ. Eng. Sci.* **2021**, *33*, 266–275. [[CrossRef](#)]
46. Aylen, J.; Albertson, K.V.; Lim, K. The Power of the Durbin Watson Test When the Regression Errors are PAR (1). *J. Stat. Comput. Simul.* **2002**, *72*, 507–516.
47. Van Rooij, R.; Timmer, W. Roughness sensitivity considerations for thick rotor blade airfoils. *J. Sol. Energy Eng.* **2003**, *125*, 468–478. [[CrossRef](#)]

**Disclaimer/Publisher’s Note:** The statements, opinions and data contained in all publications are solely those of the individual author(s) and contributor(s) and not of MDPI and/or the editor(s). MDPI and/or the editor(s) disclaim responsibility for any injury to people or property resulting from any ideas, methods, instructions or products referred to in the content.